# Effect of the TiO$_2$-carbon interface on charge transfer and ethanol photo-reforming

Enqi Bu [a,b], Xiaowei Chen [a,b], Carlos López-Cartes [c], Fernando Cazaña [d], Antonio Monzón [d], Javier Martínez-López [e], Juan José Delgado [a,b,*]

[a] Departamento de Ciencia de los Materiales, Ingeniería Metalúrgica y Química Inorgánica, Universidad de Cádiz, Campus Río San Pedro, Puerto Real (Cádiz), E-11510, Spain
[b] Instituto Universitario de Investigación en Microscopía Electrónica y Materiales (IMEYMAT), Universidad de Cádiz, Campus Río San Pedro, Puerto Real (Cádiz), E-11510, Spain
[c] Departamento de Química Inorgánica, Universidad de Sevilla, Spain
[d] Instituto de Nanociencia y Materiales de Aragón (INMA), CSIC-Universidad de Zaragoza, Spain
[e] Departamento de Ciencias de la Tierra, Facultad de Ciencias, Universidad de Cadiz, Campus Río San Pedro, Puerto Real (Cádiz), E-11510, Spain

ARTICLE INFO

ABSTRACT

Carbonaceous materials have been widely used in photocatalysis to solve the drawback of rapid electron-hole recombination rate of semiconductors such as titania. To further understand the charge separation mechanism and its effect on the ethanol photoreforming hydrogen production, two types of carbon-titania hybrid material systems were studied. One of them is multi-walled carbon nanotube-titania nanoparticles (MWCNT-TiO$_2$) prepared by a sol-gel synthesis method, which according to previous studies should facilitate the migration of electrons from TiO$_2$ to MWCNT. The second system is based on a two-dimensional carbon (exfoliated carbon, 2DC) and titania nanosheet (TNS), synthesized through a hydrothermal route that enabled the formation of strong interaction between the carbon and the {001} facets of the TNS. Our results demonstrate that this unique design promotes the migration of the photogenerated holes from the TNS to the expanded carbon. Steady state photoluminescence studies indicate that the recombination rate in both cases decreases benefiting from the spatial separation of photogenerated carriers, resulting in enhanced photocatalytic activity. The present study provides a comprehensive understanding of the charge separation mechanism and its effect on ethanol photo-reforming hydrogen production in carbon-titania hybrid material systems and clearly highlights the need for further research to investigate the charge transfer in these kinds of hybrid materials.

## 1. Introduction

With the continuous consumption of non-renewable resources and the increasingly serious environmental pollution problems caused mainly by the combustion of fossil fuels, finding a renewable environment-friendly alternative energy source is a vital need for modern society [1]. In this scenario, hydrogen has emerged as a promising candidate to replace the traditional fossil fuels such as coal, petroleum, natural gas, etc [2]. As a renewable energy source, hydrogen has a very high calorific value of combustion. Moreover, hydrogen is an environmentally friendly option as it produces only water when used as fuel. In addition, hydrogen is widely used as feedstock in many chemicals, electronics, and metallurgical industries. However, at present time, the industrial production of hydrogen primarily relies on steam reforming of methane, which is a high energy-consuming process that additionally generates CO$_2$ emissions [3]. Under this context, governments worldwide have established ambitious strategies aimed at developing efficient, economical and energy-neutral processes for sustainable hydrogen production. This development is essential for the decarbonization of our society.

Since Fujishima and Honda revealed the possibility of generating hydrogen through the splitting of water using UV light-induced electrocatalysis [4], it has been a significant interest in developing efficient solar-light-driven photocatalytic processes for sustainable hydrogen

production. Among the photocatalytic reactions reported in the literature, one of the most appealing is the liquid phase photoreforming of biomass-derived hydrocarbons, such as ethanol. This reaction occurs at ambient pressure and room temperature, and produces acetaldehyde instead of carbon dioxide. Importantly, acetaldehyde has numerous industrial applications and it can be used directly in the production of perfumes, polyester resins and basic dyes [5].

Many different semiconductors such as $TiO_2$, CdS, ZnO and $C_3N_4$, etc., have been explored for the photocatalytic hydrogen production [6, 7]. Among them, titanium dioxide ($TiO_2$) has become one of the most widely used semiconductors in photocatalysis due to its high activity, thermal and chemical stability, nontoxicity, corrosion resistance and relatively low cost [8]. Nevertheless, it also shows some limitations, including the following two main drawbacks: the fast electron-hole recombination rate and the limited range of solar light absorption due to its relatively wide band gap (ca. 3.2 eV) [9]. To solve these problems and further improve the photocatalytic activity of $TiO_2$, several strategies have been proposed, including heterojunction construction [10], metal loading (co-catalyst) [11], metal and non-metal doping [12] and coupling with other materials [13].

Carbon materials, one of the most abundant available resources worldwide, have shown unique physical, chemical, and thermal properties that make them highly attractive for catalytic applications [14]. In particular, the carbon materials have commonly been used as additives to create hybrid materials with enhanced electronic properties, which can be utilized to promote the separation of the photogenerated charge carriers and boost the photocatalytic activity [15]. Indeed, various types of carbon-based materials have been reported to exhibit higher photocatalytic activity than bare photocatalysts [16,17]. However, the most relevant studies on photocatalysis using carbon-based hybrid materials assume that carbon materials merely act as electrons acceptor/conductor. Yu et al. [18] synthesized $Cd_{0.1}Zn_{0.9}S$ modified with carbon nanotubes by a simple hydrothermal method and it showed enhanced photocatalytic activity under visible light. The authors proposed that the photogenerated electrons were transferred to the CNT due to its high electrical conductivity and long-range electronic conjugation, resulting in enhanced photocatalytic activity. Woan et al. [19] reached a similar conclusion using $TiO_2$ with multi-walled carbon nanotubes as photocatalyst. Besides, other carbon materials such as graphene [20] and fullerene [21] were also reported to capture photo-induced electrons from semiconductors, leading to charge separation and higher photocatalytic activity. On these bases, in a few studies, carbon materials are also employed as a solid state electron mediator to construct a Z-scheme heterojunction photocatalyst. Benefiting from the good conductivity of carbon materials, photogenerated electrons could migrate between two semiconductors or dye sensitized solar cells through carbon [22,23]. In contrast, very few studies have proposed completely different charge transfer pathways in carbon-composite photocatalysts. Recently, Saha et al. [24] provided evidence that the charge separation can be governed by hole transfer from the valence bands of titania to the carbon materials. Similarly, Lettieri et al. [25] revealed the hole transfer from $TiO_2$ to graphene related materials through a combined EPR, photoluminescence and photocatalysis assessment. It should be pointed out that carbon materials are commonly accepted as electron acceptors in photocatalysis. However, in other fields such as photovoltaics, it is accepted that carbon materials can act as both hole and electron acceptors [26]. Therefore, the roles and advantages of carbon materials in various photocatalyst systems still require more understanding. Special attention should be paid to the development of strategies that control the process of charge carrier transfer to reduce the recombination rate.

In this work, two strategies were implemented to promote the electron migration either from titania to the carbon material or the reverse from the carbon material to titania. It should be pointed out that the latter strategy has not been considered in the literature, and therefore one of the aims of this work is to provide evidence that this approach

may also contributes to the improvement reported in the literature. In order to achieve this objective, we have taken advantage of the morphology of different carbon materials and $TiO_2$ nanoparticles. We propose that the electron migration from the carbon material to the titania can be improved by using a two dimensional carbon material as an additive of titania nanosheets. By this approach, we successfully promote the interaction between the {001} facets of TNS, where the photo-induced holes are located, and the carbon material. Additionally, a reference MWCNT-$TiO_2$ system was obtained, where the carbon material acted as a good conductor, facilitating the migration of photo-generated electrons from $TiO_2$ to MWCNT and then achieving the spatial separation of charge carriers. Influence of the microstructure of the multi-walled carbon nanotubes on the catalytic performance was also studied by using MWCNT with different annealing pre-treatments that improve its crystallinity.

## 2. Experimental

### 2.1. Reagents and materials

All chemical reagents are analytical grade and used without further purification. Titanium (IV) butoxide (Ti(OBu)$_4$, 97%) was purchased from Sigma-Aldrich Ltd. Hydrofluoric acid (HF, 48%) was purchased from Acros Organics Ltd. 2-propanol ($C_3H_8O$, 99.5%) was purchased from PanReac AppliChem Ltd. Absolute ethanol ($C_2H_6O$) was purchased from Scharlab Ltd. Platinum nitrate (Pt(NO$_3$)$_2$, 99.95%) was purchased from chemPUR Ltd.

Commercial MWCNTs used in this study were synthesized by chemical vapor deposition (CVD) and provided by Pyrograf Products Inc. (Ohio, USA). After the CVD, the MWCNTs were treated at 700 (CNT) or 3000 (gCNT) °C under inert by the provider. The commercial names of the products are PR19-PS and PR19-HHT, respectively. In order to improve the miscibility of the gCNT in ethanol, the sample was further treated in air at 620 °C for 5 h.

The two dimensional carbon was obtained using an Expandable Graphite grade 3772 provided by Asbury Carbons. Typically, 50 mg of this raw material was placed in a beaker and then microwaved for 30 s at a power of 800 W.

### 2.2. Synthesis of MWCNT-TiO$_2$ photocatalyst

The MWCNT-$TiO_2$ was synthesized using a sol-gel method [27]. Typically, 15 mg of CNT or gCNT was suspended in 60 mL of absolute ethanol and exposed to ultrasound (120 W, Ultrasonic Cleaner, VEVOR®) to obtain a uniform suspension. Subsequently, 18 mL of Ti (OBu)$_4$ was added to the suspension under continuous stirring. After 1 h, 1.44 mL of Milli Q water was added dropwise to the mixture and kept stirring for an additional hour. The solid samples were filtrated using a nylon filter membrane with 0.45 μm pore size (Filter-Lab®). Besides, 60 mL of absolute ethanol was used to remove the residual impurities and finally the samples were dried in oven at 100 °C for 12 h. Furthermore, the samples were re-dispersed in Milli Q water and stirred at room temperature for 4 h for a second wash, followed by filtration and drying at 100 °C for 12 h. The synthesis process of bare $TiO_2$ was the same except for the adding of MWCNTs. All samples were calcined in a muffle oven at 350 or 450 °C for 6 h under air atmosphere to evaluate the effect of the $TiO_2$ crystallinity on the catalytic performance. The mass yields of the samples calcined at 350 and 450 °C were calculated to be approximately 74% and 61%, respectively.

### 2.3. Synthesis of 2DC-TNS photocatalyst

2DC-TNS was synthesized using a hydrothermal method modified from literature [28]. Initially, 5 mg of carbon was dispersed in 60 mL of 2-propanol with the assistance of ultrasound in a custom-built Teflon autoclave with a volume of 150 mL. Then 6 mL of Ti(OBu)$_4$ were added

to 2-propanol solution. Finally, 2.16 mL of HF aqueous solution (48%) was added dropwise to the autoclave. The six-port autoclaves [29] were placed in an oven and rotated with a speed of 50 rpm. The temperature of the oven was increased to 180 °C and maintained for 24 h. After the oven was cooled down to room temperature, the powder sample was separated from liquid by centrifugation (4500 rpm, 15 min) and washed with ethanol and water three times. Finally, the photocatalyst was obtained after drying at 100 °C for 12 h. The bare TNS was prepared in the same method without the addition of carbon. The mass yields were calculated to be approximately 58% for both the TNS and the 2DC-TNS. More information about the structure of the bare TNS and the synthesis can be found herein [30].

### 2.4. Photodeposition of $MnO_x$

Normally, 10 mg of sample and a calculated amount of precursor Mn $(NO_3)_2$ with a final Mn loading of 1 wt% were mixed in 70 mL of Milli Q water. Besides, $NaIO_3$ was added as the electron acceptors to facilitate the photodeposition. Then the suspension was irradiated by a 80 W LED collimator source (365 nm, MIGHTEX) under continuous stirring. After 3 h of photodeposition, the suspension was filtered and dried at 60 °C for 12 h.

### 2.5. Characterization of photocatalysts

The powder diffraction patterns of all samples were recorded using a D8 advance-A25 diffractometer (Bruker) with Cu Kα (λ = 0.154 nm) radiation source at a scanning rate of 2° min$^{-1}$. The Brunauer-Emmett-Teller specific surface area ($S_{BET}$) was determined by nitrogen adsorption-desorption in a Micromeritics ASAP 2020 apparatus. All the samples were degassed at 200 °C for 2 h prior to the surface area measurements. The temperature programmed oxidation ($O_2$-TPO) experiments were performed in a programmed heating reaction device connected to a mass spectrometer (PrismaPlus™, Pfeiffer Vacuum). A conventional experiment was carried out with 50 mg of the sample and using a flow of 60 mL/min of a 5% $O_2$ in Ar. After the stabilization of the mass spectrometer, the oven was heated up to 850 °C at a rate of 10 °C/ min. The 44 *m/z* signal was recorded to determine the $CO_2$ produced and the carbon content. Besides, a calibration of the $CO_2$ signal was performed using calcium oxalate diluted with quartz. Inductively coupled plasma-optical emission spectrometer (ICP-OES, Spectrogreen) was used to determine the element content of samples. UV-Vis diffuse reflectance spectra (DRS) were recorded using a Shimadzu UV-3600i spectrophotometer equipped with an integrating sphere. $BaSO_4$ was used as a reflectance standard during the measurement. X-Ray photoelectron spectroscopy (XPS) measurements were carried out using an Kratos Axis Ultra DLD X-ray photoelectron spectrometer. The morphology of the samples was studied by scanning electron microscopy (SEM) using a Nova NanoSEM 450 at an accelerating voltage of 5 kV. High-angle annular dark field scanning transmission electron microscopy (HAADF-STEM) images were obtained on a Talos F200X instrument. The HAADF-STEM technique is sensitive to the atomic number of the elements, whose intensity is roughly proportional to the square of the atomic number ($Z^2$) and makes possible to distinguish small nanoparticles supported on light supports. Moreover, elemental mapping was obtained using energy dispersive X-ray spectroscopy (EDX) to study the element distribution. EDX mappings were performed using a beam current of 200 pA and a dwell time per pixel of 128 μs. To minimize the electron-induced sample drift and damage, we utilized a spatially-resolved electron energy-loss spectroscopy (EELS) method in STEM mode with a Gatan Imaging Filter (GIF) Continuum integrated into the Talos microscope. The 2D spectral image (SI) data for STEM-EELS were acquired using a 2.5 mm diameter aperture and 0.15 eV/channel energy dispersion, allowing for the simultaneous acquisition of the O-K and Mn-$L_{2,3}$ signals. The energy resolution of 1.0 eV was calculated for the acquired data. For almost simultaneous acquisition of both low-loss and

core-loss signals, we used a dual-range EELS (DualEELS™) acquisition mode. This approach enabled us to correct the signal drift in each individual pixel of the SI using the zero loss peak (ZLP). Overall, the use of spatially-resolved EELS with DualEELS™ acquisition mode and ZLP correction allowed for accurate and reliable data acquisition while minimizing sample damage. To improve the visual quality of the elemental maps obtained, these were filtered using a Gaussian blur of 0.8 using Velox software. The photoluminescence (PL) spectra were collected by a fluorescence spectrometer (Horiba Fluorolog-QM) equipped with a continuous 75 W Xenon arc lamp and a photomultiplier tube (PMT) detector (920IS). The photon detection efficiency of the PMT detector and the grating was calibrated over the full range of wavelengths used and all the spectrum included in this work are corrected using this calibration to prevent error in determinate the maximum of the fluorescence emission. All the spectra were obtained at − 196 ºC under vacuum using a cryostat (CS204-FMX-1SS, ARSCRYO) that can be operated between − 268 and 40 ºC. The excitation wavelength was selected to be 325 nm and a 400 cut filter (Newport FSQ-GG 400) was used before the emission monochromator to remove artefacts in the spectra related to the second order diffraction of the excitation light that would be observed at 650 nm.

### 2.6. Hydrogen production evaluation

The photo-catalytic tests were carried out using an on-line photoreactor developed in our laboratory that allows to measure simultaneously up to four samples (Fig. S1). A solar simulator (450 W Xenon lamp, Oriel Sol3A, Newport) was used as the light source without any additional filter. The temperature of the reactor was maintained constant at 8 ºC thanks to a cooling jacket system connected to a thermostatic bath (AP7LR-20, VWR). Before and after each experiment, a spectrum of the light source was measured with a spectrometer (Flame-S, Ocean Insight) to ensure the stability of light source during the test. Fig. S2 shows a representative spectrum of the light source. In addition, a pyranometer (LP PYRA 03 AV, Delta Ohm) was also used to measure the sun light irradiance (1.68 sun). The irradiated area of the reactor was 15.2 cm$^2$. In a standard photocatalytic test, 10 mg of photocatalyst nanoparticles were dispersed in 70 mL of a 50% by volume ethanol aqueous solution that was magnetically stirred (800 rpm). Before sealing the reactor, the appropriate volume (175 μL) of a Pt$(NO_3)_2$ solution (55.6 ppm of Pt) was added in order to in-situ photodeposit Pt as a cocatalyst. The final theoretical Pt loading was 0.1 wt%, which was also confirmed by ICP-OES. After a leak test, the residual air in the reactors was purged with argon for 2 h at a flow rate of 15 mL/min. The flow was kept constant during all the experiments and it was used as carrier to analyze the products using an on-line gas chromatograph (GC Trace 1300, Thermo Scientific) equipped with a high-sensitivity thermal conductivity detector and a Carboxen 1010 PLOT Capillary GC Column. The analysis of intermediates from photocatalytic solution was carried out on a high performance liquid chromatography system (HPLC, Thermo Scientific Dionex UltiMate 3000). 0.005 N sulfuric acid in water was used as aqueous mobile phase at a flow rate of 0.5 mL/min. The column was maintained at 25 °C and the injection volume was selected to be 10 μL.

## 3. Results and discussion

### 3.1. MWCNT-TiO$_2$ system

The XRD patterns included in Fig. 1a show that all the samples exhibit diffraction peaks at 25.3°, 37.8°, 48.0°, 53.9°, 55.1°, 62.8° and 75.1°, corresponding to planes (101), (004), (200), (105), (211), (204) and (215) of anatase TiO$_2$ (JCPDS No.73–1764). No additional signals of other crystal phases were observed, confirming that pure anatase was obtained after the calcination treatment and that the carbon material did not affect the crystallinity of titania. No apparent MWCNT peaks in the
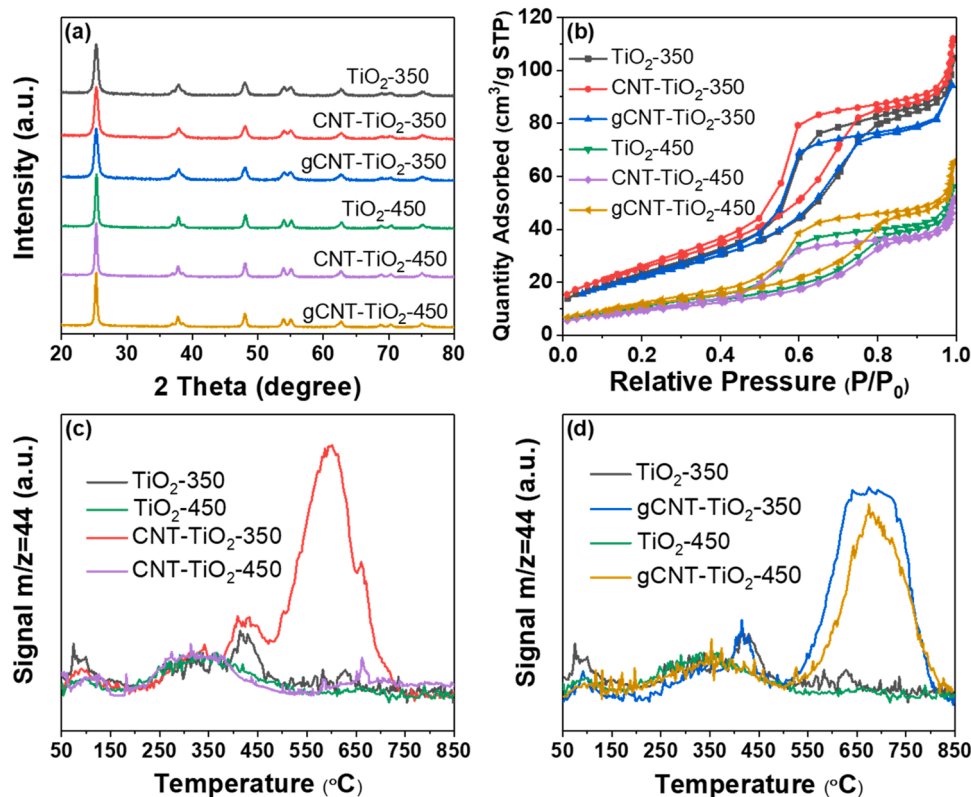
**Fig. 1.** (a) XRD patterns, (b) $N_2$ adsorption-desorption isotherms, (c) and (d) $O_2$-TPO profiles of $TiO_2$, $CNT$-$TiO_2$ and $gCNT$-$TiO_2$ calcined at 350 and 450 °C.

$CNT$-$TiO_2$ samples could be observed, indicating that the final carbon contents are low. The corresponding crystallite size was calculated by Rietveld analysis of the diffractograms using the software TOPAS 5.0 (Bruker AXS). As displayed in Table 1, the particle size of the bare $TiO_2$ calcined at 350 °C was estimated to be 21.8 nm, and after calcination at 450 °C, it almost doubled to 34.5 nm. It is evident that particle sintering is promoted by increasing the calcination temperature. Similar results were obtained when CNT is added, so apparently the presence of MWCNTs does not improve the thermal stability of the sample. Fig. 1b displays the nitrogen adsorption-desorption isotherms. All samples exhibited a typical type IV isotherm with a type H2 hysteresis loop (IUPAC classification) at a relative pressure from 0.5 to 0.8, indicating the presence of mesopores caused by stacking of particles [31]. Based on the results presented in Table 1 and Fig. 1b, it can be concluded that the

addition of a small amount of MWCNTs did not lead to significant changes in the pore structure and specific surface area. However, the specific surface area of all samples calcined at 350 °C was more than 2 times higher than that of samples calcined at 450 °C, which is consistent with the obtained crystallite size by XRD.

$O_2$-TPO was performed to quantify the carbon content and its nature, and the resulting $CO_2$ signal profiles are presented in Fig. 1c and d. It was observed that all the samples exhibit some small $CO_2$ release at low temperature (below 400 °C), which is likely due to the adsorption of atmospheric $CO_2$ on the surface of the samples during storage. Additionally, a small peak centered around 425 °C was detected in all samples calcined at 350 °C, including the bare $TiO_2$ sample, which may be attributed to residual organic precursors used in the synthesis. This peak was absent in the samples calcined at 450 °C, possibly indicating complete removal of the precursors during calcination. We can also observe a peak centered at 600 °C in the $O_2$-TPO of the low graphitized MWCNT sample calcined at 350 °C, which can be attributed to the combustion of the MWCNTs. In fact, no water release was accomplished to the $CO_2$ production. Interestingly, the sample calcined at 450 °C does not display this peak, indicating that the MWCNTs were likely combusted during the calcination of the sample. In the case of the samples containing highly ordered MWCNTs, the $CO_2$ production associated to the MWCNTs is centered at a higher temperature as a consequence of the higher graphitic structure. Interestingly, the combustion of the raw MWCNTs occurs at much higher temperature (664 °C and 810 °C) (Fig. S3), which is an evidence of the good interaction between MWCNTs and the titania. In this case, the titania catalyzes the combustion of the MWCNTs. The area of this peak was used to determine the final carbon content of the samples (Table 1). Similar carbon contents were found in the samples calcined at 350 °C (0.16–0.18%), but after calcination at 450 °C almost all of the poorly crystalline MWCNTs were burned. In contrast, approximately 66% of the gCNT remained in the sample after the highest temperature treatment. The carbon content has an obvious effect on the color of the samples, which can be observed in the picture

**Table 1**
The summarization of various characteristic parameters obtained from analysis of $TiO_2$, $CNT$-$TiO_2$ and $gCNT$-$TiO_2$ calcined at 350 and 450 °C.

|  | X-Ray Analysis | | Light Absorption | Nitrogen Adsorption Analysis | | | TPO |
|---|---|---|---|---|---|---|---|
|  | (101) | | Band Gap | $S_{BET}$ | PV | PS | Carbon |
|  | 2θ | nm | eV | $m^2/g$ | $cm^3/g$ | nm | wt% |
| $TiO_2$-350 | 25.29 | 21.8 | 3.26 | 81.3 | 0.17 | 6.9 | - |
| $CNT$-$TiO_2$-350 | 25.30 | 21.0 | 3.24 | 93.1 | 0.18 | 6.3 | 0.16 |
| $gCNT$-$TiO_2$-350 | 25.29 | 20.2 | 3.23 | 81.3 | 0.18 | 6.8 | 0.18 |
| $TiO_2$-450 | 25.32 | 34.5 | 3.24 | 36.2 | 0.09 | 7.7 | - |
| $CNT$-$TiO_2$-450 | 25.31 | 35.6 | 3.24 | 33.7 | 0.09 | 7.5 | 0.03 |
| $gCNT$-$TiO_2$-450 | 25.31 | 35.5 | 3.22 | 42.1 | 0.11 | 7.5 | 0.12 |

included in Fig. S4. Visual observation of the samples revealed that CNT-TiO$_2$-350, gCNT-TiO$_2$-350 and gCNT-TiO$_2$-450 displayed a similar dark gray color. However, CNT-TiO$_2$-450 appeared a much lighter color, but it was still not as white as the bare TiO$_2$, indicating the presence of a trace amount of carbon (not detected by the TPO experiments), and that strongly affects the color of the sample.

SEM images of the catalysts under the same magnification are included in Fig. 2a and Fig. S5. We can observe that the bare TiO$_2$ calcined at 350 ºC and 450 ºC (Fig. S5) show big particle agglomerates ranging from 1 to 5 µm in size. Similar TiO$_2$ particle aggregates can be observed in the carbon-containing catalysts, although in this case we can identify MWCNTs with an outer diameter ranging from 60 to 150 nm that are partially covered by TiO$_2$ nanoparticles. It is impossible to determine the presence of MWCNTs inside of the TiO$_2$ agglomerations by this technique. Thanks to the combination of EDX and STEM techniques, it was possible to obtain element mapping and confirm the presence of this MWCNTs inside of the TiO$_2$ agglomerations (Fig. S6). Nonetheless, the partially covered carbon surface might be more favorable for the deposition of Pt particles, which would eventually promote the diffusion of the reactants to its surface. The only exception was the sample CNT-TiO$_2$-450, where MWCNTs could not be found by SEM. This could be explained by the very low carbon content obtained from the TPO results. For this sample, HAADF-STEM technique allowed us to identify the presence of nanotubes formed by TiO$_2$ nanoparticles (Fig. 2b). These nanotubes are believed to be formed by the combustion of MWCNTs that were coated by TiO$_2$ nanoparticles, where the MWCNTs act as a hard-template for this structure. Similar structures were also found in the sample gCNT-TiO$_2$-450, but it was less common since most of the MWCNTs remained in the sample after the calcination step (Fig. S7).

The high resolution XPS spectrum of the C 1s was studied to investigate the chemical properties of the carbon present in the prepared nanocomposites. It must be pointed out that the carbon analysis by XPS is difficult due to the so called adventitious carbon layers, which is commonly used as a binding energy (BE) reference in X-ray photoelectron spectroscopy studies. We can observe that the signal of the bare TiO$_2$ can be deconvoluted into the following contributions: 284.8 eV, 286.3 eV, 287.8 eV and 288.8 eV. These binding energies correspond to the C-C, C-OH, C=O and HO-C=O groups, respectively [32,33]. As we can observe in Fig. 3 and table S1, these peaks are present in all the samples, indicating the existence of the previously mentioned

adventitious carbon layer. However, we can reach two interesting conclusions of this analysis. The first one is that a similar C 1s signal is obtained in all the cases, suggesting a relatively low contribution from the MWCNTs, which can be an indication that the MWCNTs are well-covered by the TiO$_2$ particles. In fact, previous studies indicate that these raw MWCNTs display a single peak at 284.5 eV, which is the main contribution that increases in the MWCNTs containing samples [34]. The second deduction is that an additional weak peak at 283.7 eV is observed in the samples with higher carbon contents (CNT-TiO$_2$-350, gCNT-TiO$_2$-350 and gCNT-TiO$_2$-450). According to Bellamkonda et al., this peak can be attributed to the strong chemical coupling C-Ti [35], which is formed by the hydrolysis of titanium alkoxides that are adsorbed on the surface of MWCNTs during the synthesis process. These results also indicate the good interaction between the MWCNTs and the TiO$_2$ nanoparticles.

The optical absorption properties of the samples were investigated using UV-Vis DRS spectroscopy. The reflectance spectra of all the samples are shown in Fig. 4a and we can conclude that all the samples exhibited an absorption edges at ca. 410 nm. Compared with the TiO$_2$ nanoparticles, the absorption edges of the MWCNTs-containing samples are almost the same, suggesting that the addition of MWCNTs did not modify the band structure of the titania. In fact, considering the band gap (Formula S1) obtained from the plot in Fig. 4b and listed in Table 1, the addition of a small amount of MWCNTs did not significantly modify this parameter. Nevertheless, the TiO$_2$–CNTs composites exhibited a characteristic UV–Vis spectrum with a widened and virtually constant absorption that extends over almost the entire visible region, which can be ascribed to the absorption properties of MWCNTs. It has been previously reported that carbon materials are capable of absorbing light over a wide continuous range of wavelengths in the visible region [36, 37]. The CNT-TiO$_2$-350 and gCNT-TiO$_2$-350 showed nearly the same ability of light absorption in the visible range, while gCNT-TiO$_2$-450 displayed weaker visible light absorption capabilities. Interestingly, CNT-TiO$_2$-450 showed a similar reflectance profile to the raw titania materials, although the reflectance from 410 to 700 nm was 80%. This suggests the presence of a small amount of MWCNTs, as inferred from the color of the sample, even though it was below the detection limit of our MS. Therefore, the correlation between the carbon content and the absorption properties of the samples at the visible range is clear [38].

Steady state photoluminescence technique is widely used in the literature to rationalize the photocatalytic results. It is commonly
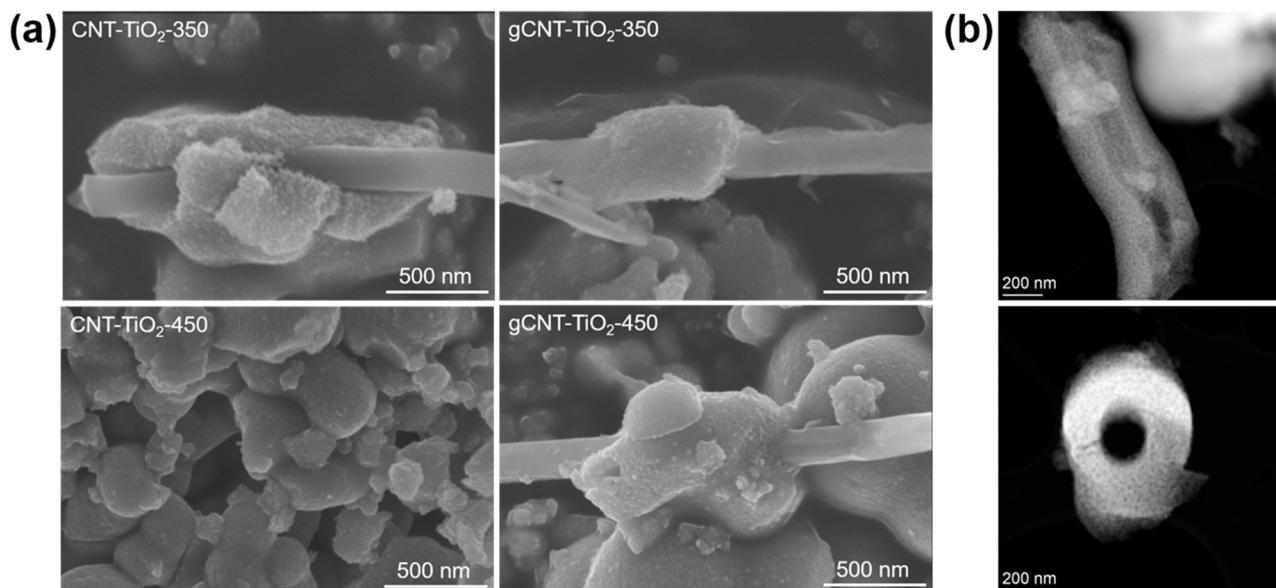


**Fig. 2.** (a) SEM images of CNT-TiO$_2$-350/450 and gCNT-TiO$_2$-350/450 under the same magnification and (b) HAADF-STEM images of CNT-TiO$_2$-450.
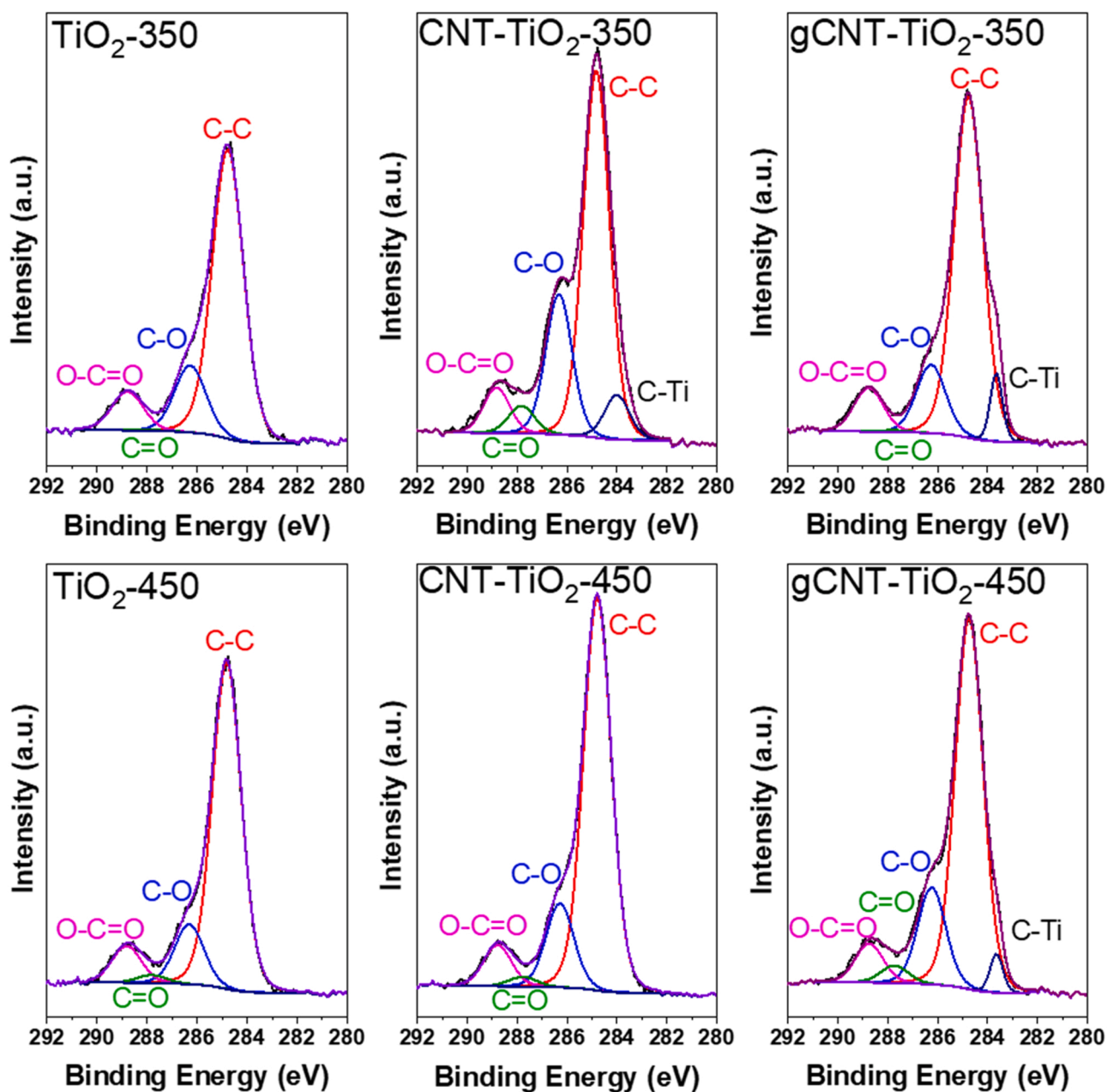
**Fig. 3.** High resolution C 1s XPS spectra of $TiO_2$, $CNT\text{-}TiO_2$ and $gCNT\text{-}TiO_2$ calcined at 350 and 450 °C.
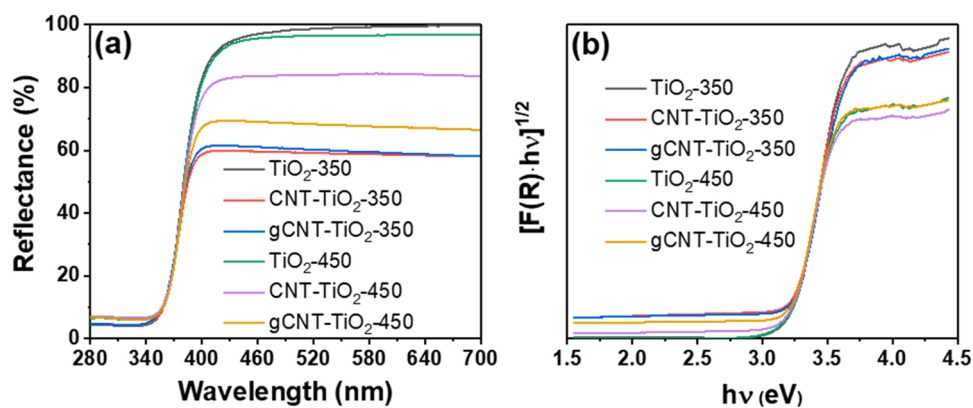


**Fig. 4.** (a) UV-Vis diffuse reflectance spectra and (b) band gap energy of $TiO_2$, $CNT\text{-}TiO_2$ and $gCNT\text{-}TiO_2$ calcined at 350 and 450 °C.

accepted that high PL signals are consequence of a fast hole/electron recombination rate, which reduces the efficiency of the photocatalyst in utilizing the energy of the photons from the light source to carry out a chemical reaction. Despite its importance, it is surprising that numerous papers show notable errors in their interpretation, and even more worrying, the spectra were recorded using inappropriate conditions. It is worth to mention the excellent work conducted by Professor Jeanne L. McHale and her group in this field, who pointed out this problem in the literature in an inspiring work published in 2013 [39]. This work clearly shows the difficulties of using conventional fluorimeters to record the titania photoluminescence spectrum. Conventionally, the PL acquisition is carried out using commercial PL spectrometer at room temperature and in air. However, under these conditions, the PL emission of titania is quite weak mainly due to the strong efficiency of the molecular oxygen in scavenging photo-excited electrons. As a result, the recorded spectra are often not the PL of the titania and may be misinterpreted due to the weak scattering of the Xe lamp emission passed by the excitation monochromator. The signal can be improved by removing the oxygen and eventually reducing the temperature of the sample. For this reason, all the results included in this work were performed under vacuum at $-196\ ^\circ$C. Fig. 5 shows that all the spectra have an apparent wide peak center between 530 and 575 nm. Accordingly, consistent with the literature, the fluorescence emission from anatase nanoparticles can be regarded as the result of the overlapping of two peaks in the green and red regions of the spectra. The first peak can be assigned to the recombination of photo-excited electrons with trapped holes, while the second is related to the recombination of trapped electrons with valence band holes [40]. The green emission peak can be directly related with the oxygen vacancies in our sample. We can observe that the position of the highest intensity shifts to lower wavelengths after calcining the samples at 450 °C, which can be attributed to a higher content of oxygen vacancies even though the fact that the calcination treatment should reduce the amount of oxygen vacancies. Another plausible explanation is that the amount of electron traps responsible for the red emission has decreased after the calcination at high temperature. In the case of titania, electron traps are mainly associated to $Ti^{3+}$-OH on the surface of the sample [41]. If we consider that the calcination treatment at 450 °C dramatically decreases the specific surface of the samples, it is logical to assume that these groups have been partially removed and that the emission at higher wavelengths will be attenuated. This would provoke the observed peak shift to higher energy. Interestingly, the sample with highly ordered MWCNTs has the maximum of the peak at the lowest wavelength and the contribution of the high wavelength emission is lower. It is commonly accepted that low fluorescence intensity leads to worse recombination efficiency of electron-hole pairs, which benefits the photocatalytic activity. However, it should be noted that, according to our UV-Vis absorption results, the samples with MWCNTs can absorb a wide range of the visible light. Therefore, it is reasonable to assume

that an undetermined fraction of the radiation emitted by the sample could be reabsorbed. However, considering that the absorption from 450 nm up to 700 nm is almost constant, it can be inferred that this reabsorption would impact the intensity rather than the shape of the spectra.

Photoreforming hydrogen production experiments were performed to evaluate the catalytic activity of all the materials. As shown in Fig. 6, the hydrogen production rate of all samples reached a maximum value after ca. 0.5 h and then kept stable. No obvious deactivation could be observed during the photocatalytic tests. We can observe that the samples calcined at low temperature exhibit higher activities. In fact, the catalytic performance of all the samples was negatively affected by calcination at 450 °C, although being more significantly impacted in the case of the bare titania. This observation is traditionally ascribed to the increase in particle size, which grows from around 22–34 nm. However, despite the similar increase in particle size of all the samples after calcination at 450 °C, the effect on the photocatalytic activity is less pronounced when MWCNTs are used and negligible in the case of highly ordered CNTs-TiO$_2$ composites. CNT-TiO$_2$-350 and gCNT-TiO$_2$-350 samples showed closer hydrogen production activities and they have similar amounts of MWCNTs. Fig. S8 displays the differences of microstructure between CNT and gCNT raw materials. Based on the comparison of the samples calcined at 350 °C, it appears that the MWCNT content is more influential than its nature. However, this microstructure is also responsible for the high stability of the gCNT when the sample is calcined at 450 °C. As a result, the catalytic activity of the gCNT-TiO$_2$ is not significantly affected by the calcination. In addition, it can be observed that the samples with lower activity also exhibited higher fluorescence emission in Fig. 5. In fact, the total fluorescence emission of
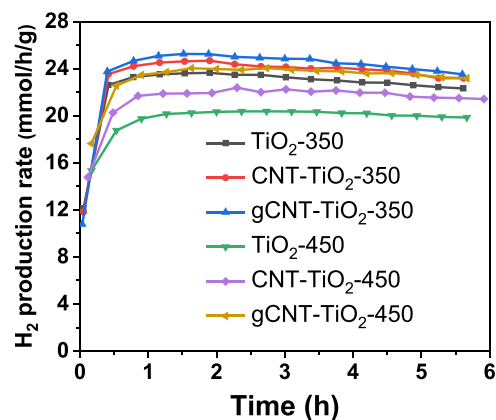


**Fig. 6.** Photocatalytic hydrogen production rate of TiO$_2$, CNT-TiO$_2$ and gCNT-TiO$_2$ calcined at 350 and 450 °C.
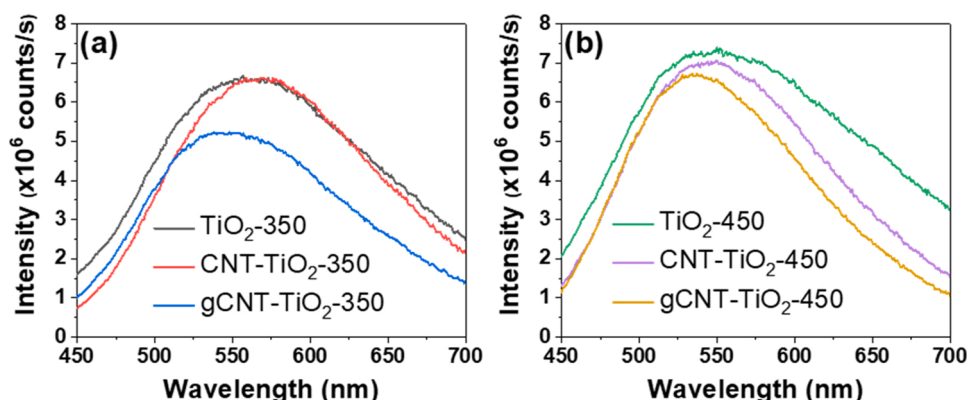


**Fig. 5.** PL emission spectra of TiO$_2$, CNT-TiO$_2$ and gCNT-TiO$_2$ calcined at (a) 350 °C and (b) 450 °C.

the samples, considering the full spectra, increases with an increase in the calcination temperature.

In order to further explore the transfer path of photogenerated charges, the samples after the photocatalytic tests were collected and studied by HAADF-STEM. Since $Pt^{2+}$ will be in situ reduced to Pt by photogenerated electrons on the catalyst surface during photocatalysis, the location of electron accumulation can be determined by the position of photodeposited Pt particles. As shown in Fig. 7, the MWCNTs in gCNT-TiO$_2$-350 were partially covered by TiO$_2$ particles, and a small fraction of Pt particles could be observed on TiO$_2$. However, it can be seen from the high resolution image of selected region that many Pt nanoparticles could be found on the exposed surface of MWCNTs, indicating that most of the photogenerated electrons were transferred to the MWCNTs. This result depends on the observed area, in the areas without MWCNTs we can easily find Pt particles on titania nanoparticles, which is obvious because electrons can only migrate on the TiO$_2$ surface without the presence of carbon tubes as electron acceptors. Similar phenomena could also be observed in other samples, except for the CNT-TiO$_2$-450 (Fig. S9). Since most of the MWCNTs in CNT-TiO$_2$-450 were burned off, Pt particles would be only deposited on the surface of TiO$_2$ rather than on the surface of MWCNTs. The results obtained at 350 ºC and 450 ºC show how the synthesis protocol strongly influences the catalytic performance and how difficult it is to unequivocally determine the beneficial effects of adding MWCNTs. If we consider the results of the samples calcined at 350 ºC, the improvement of adding MWCNTs is small, although this enhancement is significant when we analyze the data obtained after calcination at 450 ºC. On the other hand, to identify the location of photo-generated holes in this carbon-titania system, photo-oxidation experiments of $Mn^{2+}$ were conducted. According to Li et al. [42], $Mn^{2+}$ can be oxidized by the photo-generated holes and deposited as $MnO_x$ on the surface where the holes accumulate. Fig. S10 displays the Mn concentration (determined by ICP) in the solution at the end of these experiments. It can be observed that for pure carbon materials, most of the manganese still remained in solution after the reaction, indicating that these materials are not effective at oxidizing $Mn^{2+}$. The loss of Mn could be attributed to physical or chemical adsorption on the surface of these carbon materials. In contrast, the titania-based hybrid materials containing CNTs or gCNTs were able to almost completely eliminate the manganese from the solution. STEM imaging and elemental mapping of CNT-TiO$_2$-350 in Fig. 8 reveal that $MnO_x$ is distributed on the TiO$_2$ surface rather than on the surface of CNT. In order to corroborate this, EDX spectra were obtained from two areas: one mainly consisting of TiO$_2$ (orange square) and another containing only a MWCNT region (green square). The results show that no Mn was found in the area associated with MWCNT, while a content of 5.2% of Mn (Mn/(Mn+Ti)) was detected in the region where the titania nanoparticles are located. In addition, EELS experiments were

performed on one TiO$_2$ nanoparticle where the manganese was observed to determine the oxidation state of the manganese. The analysis of the white lines of Mn obtained by EELS (Fig. S11) clearly shows a similar shape and position to those obtained for a $Mn_2O_3$ reference sample. The O-K edge is slightly different from the $Mn_2O_3$ reference sample, but it is due to the fact that the analyzed area is a mixture of anatase and manganese oxide, and therefore the oxygen signal has contributions from both phases. According to Gloter et al. [43], the O-K edges of anatase exhibit several peaks between 531 and 545 eV, which correspond to the additional peaks observed in Fig. S11. These results demonstrate that manganese is oxidized by the photo-generated holes in the titania, which is in agreement to the literature [44]. A similar distribution of $Mn_2O_3$ could be also observed in gCNT-TiO$_2$-350 (Fig. S12), suggesting that photogenerated holes would mainly accumulate on the surface of TiO$_2$ during the photocatalytic oxidation of $Mn^{2+}$ using this carbon-titania system. The only difference with CNT-TiO$_2$-350 is that in very few cases manganese was found on the MWCNTs, as it can be seen in Fig. S13. This shows the possibility, even for this hybrid material, of hole migration from the titania to the carbon material, which strongly depends on TiO$_2$-carbon interface. According to our results, this synthesis approach clearly promotes the migration of electrons to the carbon material.

The above discussed results allow us to conclude that the enhancement mechanism of this photocatalyst system in photoreforming hydrogen production could be understood following the reaction scheme illustrated in Fig. 9. For bare TiO$_2$, when it is irradiated, the electrons will be excited to the conduction band (CB) and generate corresponding holes in the valence band (VB). Thus the electrons can be used to initiate reduction reaction and the holes can be used for oxidation reaction. The presence of MWCNTs in the sample will allow the electrons transfer from TiO$_2$ to the surface of MWCNTs due to the excellent electron mobility of MWCNTs. Therefore, as it was clearly demonstrated in the above discussion, at the first step of the reaction, the $Pt^{2+}$ in the solution will be reduced by those electrons located in the MWCNTs and the Pt nanoparticles will be predominantly deposited on the surface of MWCNTs. Subsequently, the photogenerated electrons will be continuously transferred from TiO$_2$ to the Pt through the MWCNTs and will be used in the reduction half-reaction of the photoreforming process [45]. Meanwhile, the ethanol in solution will be oxidized to the corresponding oxidation product, which in this case was mainly acetaldehyde and acetic acid according to the HPLC analysis of the solution, by the holes that are probably located on TiO$_2$ surface [46]. Therefore, the spatial separation of photogenerated electrons and holes will be achieved, thereby promoting the photocatalytic performance following the most common explanation in the literature: "electron injection from the titania to the MWCNTs" [47].

### 3.2. 2DC-TNS system

XRD patterns of TNS and 2DC-TNS are presented in Fig. 10a. All the samples showed the characteristic peaks of anatase TiO$_2$ (JCPDS No. 84–1285) at 25.3°, 37.8°, 48.1°, 53.9°, 55.1°and 62.7°, corresponding to (101), (004), (200), (105), (211) and (204) crystal family of planes, respectively. It is worth noting that, as has been previously reported [30], the bare TNS diffractogram shows that some reflections, such as those corresponding to (103), (004), (112) and (105), are considerably wider and smaller than expected. Moreover, the (200) reflection is very sharp and more intense than expected. This result is directly affected by the morphology of the TNS because the intensity of the (004) and (200) reflections can be related to the thickness and length of the nanosheets, respectively. Table 2 presents the particle size obtained using the indicated diffraction peak and the LVol-IB approach of Topas 5.0. According to these results, the crystal size is around 3.5 times bigger when considering the (200) family of planes that generate the {001} facets. When comparing the diffractogram of the bare TNS with the one obtained for the composite, we realize that the intensity of the peaks
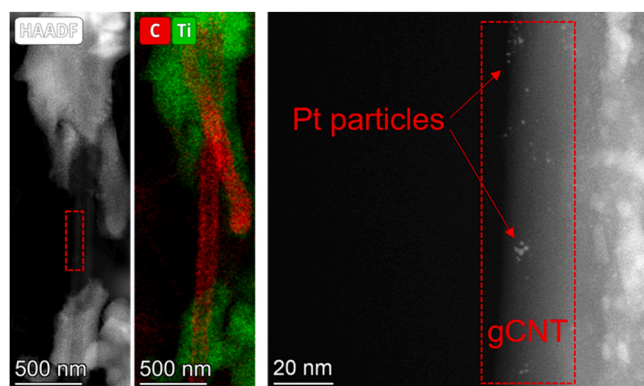


**Fig. 7.** HAADF-STEM image, corresponding element mapping and high magnification image of the selected area of gCNT-TiO$_2$-350 after photocatalytic test.
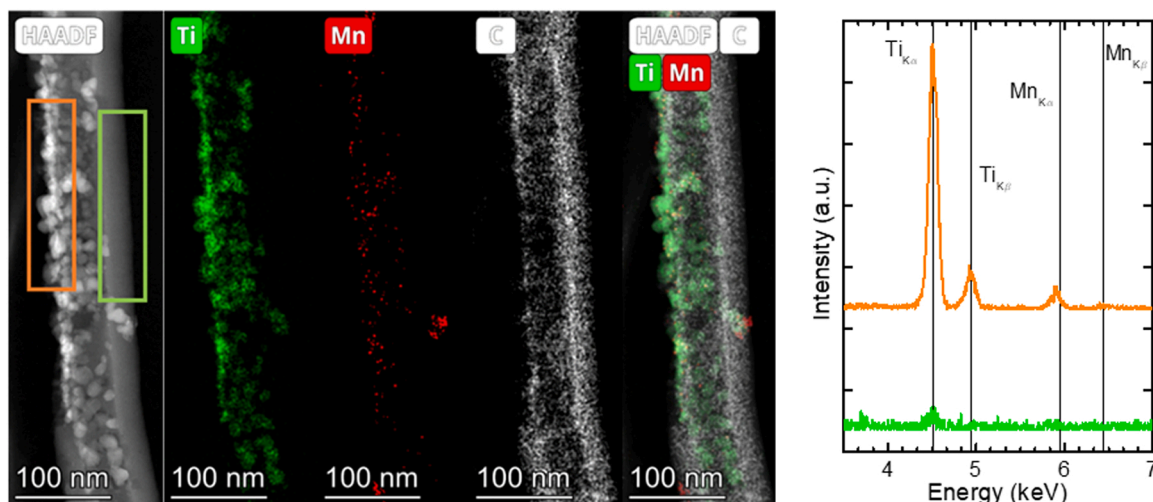
**Fig. 8.** HAADF-STEM image, corresponding element mapping and EDX of selected regions of CNT-TiO$_2$-350 after MnO$_x$ photodeposition.
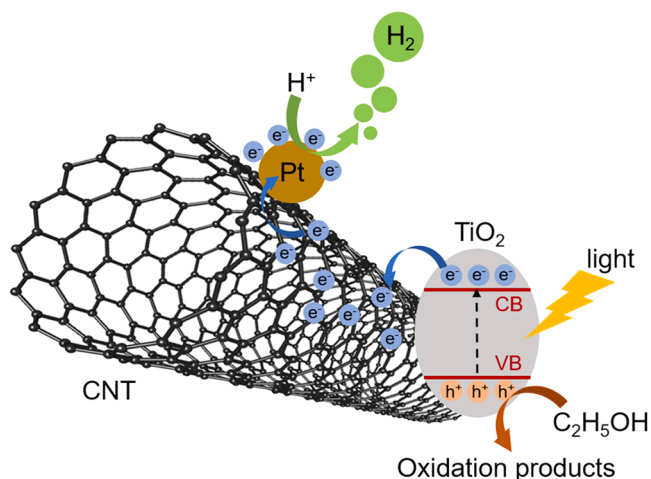


**Fig. 9.** The proposed mechanism for the photocatalytic improvement over MWCNT-TiO$_2$ system.

corresponding to (200) is slightly smaller, indicating a smaller size of the TNS along the <010> axis zone. The data included in Table 2 corroborates that the thickness of the TNS decreases to 4.9 nm, while the length increases to 34.0 nm. HAADF-STEM images of this sample included in Figs. 10b and S14 clearly show that even though the predominant facet is the {001}, the morphology of the TNS supported on the exfoliated carbon has slightly changed. Specifically, we can observe that some of them are more rectangular and the edge are rounded. These images also show that frequently the {001} surface of the TNS is in good contact with the 2D carbon. It should be recalled that the main objective of this work was to evaluate the possibility of improving the hole migration from the titania to the carbon material. It has been previously demonstrated in the literature that after photoinduced charge separation, the holes mainly accumulate on the {001} surface of the TNS, while the electrons are predominantly located at the {101} [48,49]. Therefore, the main synthetic objective of this work has been accomplished thanks to the good contact between the carbon material and the hole-rich {001} surface of the TNS.

From the nitrogen adsorption-desorption isotherms shown in Fig. 10c, both samples exhibited a type IV isotherm and a type H3 hysteresis loop at high relative pressure, indicating the existence of mesopores. Besides, the BET specific surface area of TNS was calculated as 93 m$^2$/g and increased to 112 m$^2$/g when combined with carbon

material. The BET surface area of the raw expanded carbon was only 30.0 m$^2$/g and therefore it was not expected that the BET of the composite material would increase. This result confirms that the presence of the expanded carbon in the synthesis media induces a slight modification of the morphology. Fig. 10d displays the 44 $m/z$ signal of O$_2$-TPO experiments carried out with TNS and 2DC-TNS catalysts. We can observe that the bare TNS doesn't have any relevant CO$_2$ release. On the other hand, the 2DC-TNS composite exhibits a broad peak from 220° to 475 °C, which is not observed in the case of the bare TNS and the exfoliated carbon (Fig. S15). Additionally, the main peak observed at ca. 800 °C can be attributed to the combustion of the exfoliated carbon. Unlike when MWCNTs are used, the maximum of the peak is similar to that observed for the raw exfoliated carbon. However, it is noteworthy that the combustion starts at a much lower temperature in the composite material, probably due to the fact that the TNS acts as a catalyst during the oxidation of the carbon material.

XPS analysis was performed on both catalysts and the summary of the quantitative analysis is included in Table S1. We can observe that the fluorine content of both samples is very similar and therefore it is not expected that the photocatalytic performance will be significantly modified by this parameter. The XPS C 1s spectra obtained for TNS and 2DC-TNS are shown in Fig. 11. It is noticeable that the TNS also shows a considerable contribution of carbon on the surface due to the adventitious carbon layers. This is similar to the MWCNTs based catalyst and then complicates the analysis. However, there is a relevant peak at 283.7 eV, which we previously discussed, can be related to the strong chemical coupling C-Ti [35]. This is an indication that the interaction between carbon and the titania is stronger, probably due to the intimate interaction between the carbon material and the {001} surface of the TNS. Additionally, as this synthetic route avoids the calcination of the sample, the carbon content obtained by integrating the CO$_2$ signal of the TPO was 0.9%, approximately four times higher than in the case of the MWCNT-TiO$_2$ samples.

As shown in Fig. 12a, TNS exhibited a typical anatase absorption curve with an absorption edges at ca. 410 nm. Besides, the band-gap was obtained by assuming an allowed indirect transition. Fig. 12b shows the Tauc's plot for both samples, and the band gap values for the as-synthetized TNS and 2DC-TNS samples were determined to be 3.19 and 3.16 eV, respectively. Those values are very similar and slightly smaller than the value reported in the literature for pure anatase (3.2 eV), which may be due to the presence of F in the samples [50]. The main difference between both absorption spectra relays on the absorption of the 2DC-TNS in the visible region, mainly thanks to the contribution of the carbon material. Nevertheless, the formation of the hybrid catalyst only slightly reduced the calculated band gap. In addition, as
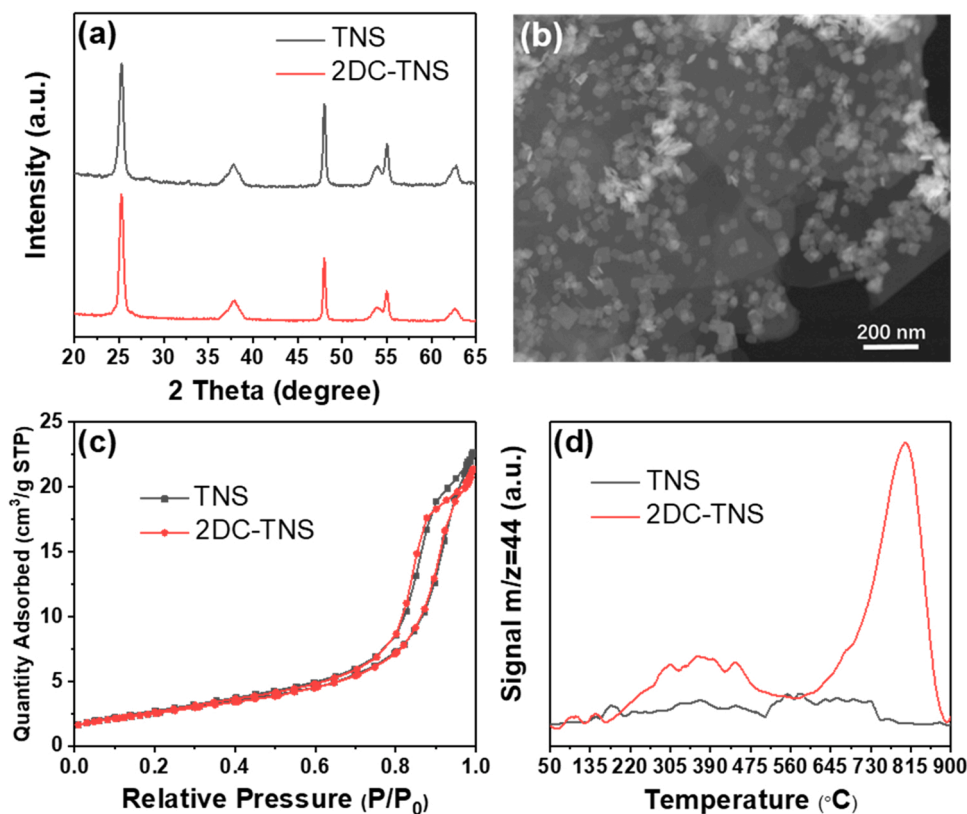
**Fig. 10.** (a) XRD patterns, (b) STEM-HAADF image of 2DC-TNS, (c) $N_2$ adsorption-desorption isotherms and (d) $O_2$-TPO profiles of TNS and 2DC-TNS.

**Table 2**
The summarization of various characteristic parameters obtained from analysis of TNS and 2DC-TNS.

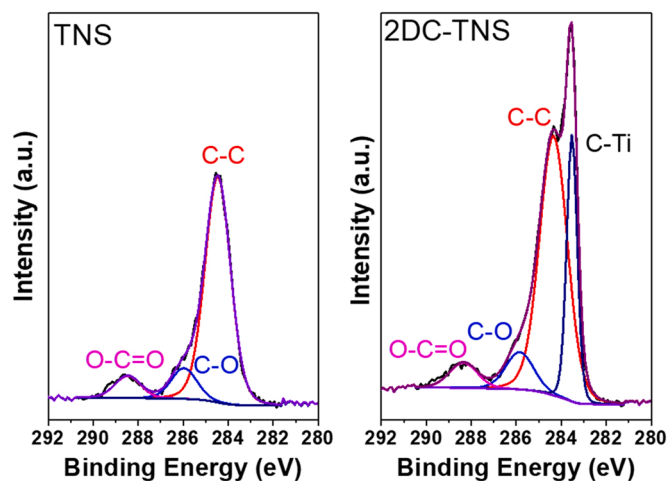| | X-Ray Analysis | | | | Light Absorption | Nitrogen Adsorption Analysis | | | TPO |
|---|---|---|---|---|---|---|---|---|---|
| | (004) | | (200) | | Band Gap | $S_{BET}$ | PV | PS | Carbon |
| | $2\theta$ | nm | $2\theta$ | nm | eV | $m^2/g$ | $cm^3/g$ | nm | % |
| **TNS** | 37.84 | 8.2 | 48.05 | 27.3 | 3.19 | 93.0 | 0.33 | 6.8 | - |
| **2DC-TNS** | 37.80 | 4.9 | 48.00 | 34.0 | 3.16 | 112.2 | 0.38 | 7.6 | 0.9 |



**Fig. 11.** High resolution C 1s XPS spectra of TNS and 2DC-TNS.

shown in Fig. 13, both samples exhibited a PL peak at ca. 545 nm and the PL intensity of 2DC-TNS was much lower than that of TNS. All these results indicate that recombination rate of the photogenerated charge

separation is smaller. Attending to the strong interaction of the carbon material with the {001} surface of the TNS, we can assume that this phenomenon can be ascribed to the hole migration from the titania to the carbon.

The photocatalytic performance of TNS and 2DC-TNS is presented in Fig. 14. Both photocatalysts reached the maximum value of $H_2$ rate in ca. 0.5 h. The $H_2$ production rate of TNS stabilized at ca. 8 mmol/h/g without deactivation, while the $H_2$ rate of 2DC-TNS was up to ca. 11.5 mmol/h/g. In contrast, the photocatalytic activity of the bare TNS and the composite is almost half that of the catalyst reported in the previous section. However, the improvement reached by incorporating the exfoliated carbon to the TNS is greater than that observed when adding the MWCNTs. Indeed, after 6 h of photocatalytic reaction, the total amount of hydrogen production over 2DC-TNS reached 66.41 mmol/g, which was 1.4 times higher than that of TNS (47.8 mmol/g). Furthermore, the samples after photocatalytic reaction were collected and studied by HAADF-STEM technique. As shown in Fig. 15, the internal interaction between the TNS remained intact after the photocatalytic tests. Moreover, Pt nanoparticles were mainly observed at the edges of the TNS and only a few (15%) were found on the carbon surface. This provides clear evidence that the photo-excited electrons predominantly stayed in the TNS and only a small fraction of them migrated to the carbon during the reaction. Therefore, it can be concluded that the improvement of the photocatalytic activity cannot be
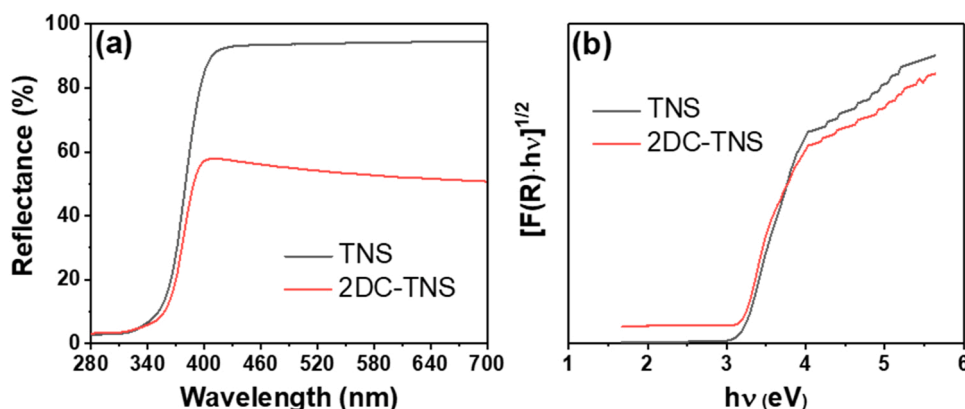
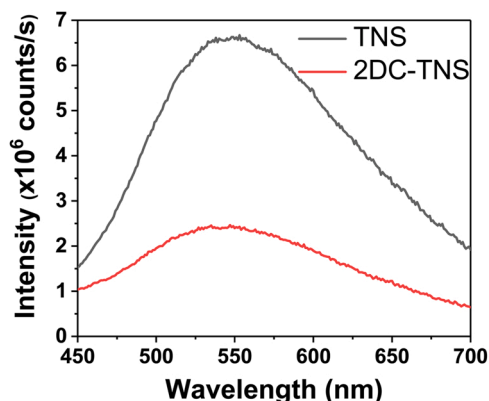**Fig. 12.** (a) UV-Vis diffuse reflectance spectra and (b) band gap energy of TNS and 2DC-TNS.



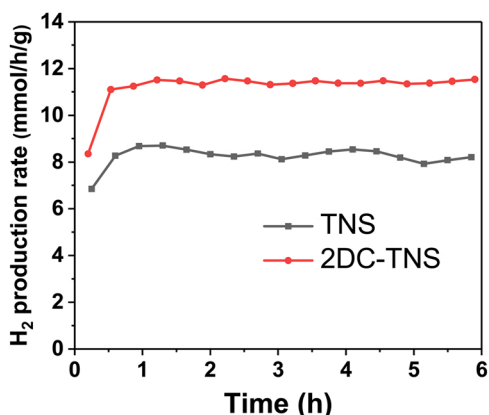**Fig. 13.** PL emission spectra of TNS and 2DC-TNS.



**Fig. 14.** Photocatalytic hydrogen production rate of TNS and 2DC-TNS.

ascribed to the assumption that carbonaceous materials can only act as electron acceptors and the electron migration of the 2DC should be considered [51]. This electron transfer may occur either from the valence band of the 2DC or activated by a sensitization mechanism [47]. It has to be mentioned that even pure 2DC is active in the photocatalytic hydrogen production (Fig. S16) under the same conditions, although its activity is very low compared to 2DC-TNS (about 0.4% of that of 2DC-TNS). In addition, the sample after reaction was studied by HAADF-STEM and Pt was found deposited on the surface of 2DC (Fig. S17), indicating that 2DC can also act as electron donor. These results indicate that this carbon material can generate corresponding electron-hole pairs when illuminated, which is also consistent with what

has been described in some literature [52,53]. In this case, the TNS sensitization by 2DC cannot be totally excluded. But considering its such low activity and the unfavorable photon shielding effect of 2DC on TNS, we could conclude that the sensitization is probably not the main mechanism for the electron transfer and the subsequent enhancement of the activity of 2DC-TNS.

To further demonstrate this idea, $MnO_x$ photodeposition experiments were performed using 2DC-TNS and 2DC samples. Fig. S10 shows that the 2DC material is not able to photo-oxidize $Mn^{2+}$, while the addition of $TiO_2$ results in the elimination of almost all the manganese of the solution. From Fig. 16, it can be observed that $Mn_2O_3$ is distributed not only on the surface of TNS, but also on the surface of carbon located relatively far from any $TiO_2$ nanoparticle. Therefore, we can conclude that the photo-generated holes accumulate on both the {101} facets of TNS and the surface of 2DC. This interesting phenomenon is different from that observed in the MWCNT-TiO_2 system and clearly shows that in this case, the carbon material acts as an anode where the oxidation half-reaction takes place. Thanks to the EELS (Fig. S11) collected in the manganese deposited on the 2DC, we can conclude that $Mn^{2+}$ has been oxidized to $Mn^{3+}$.

Based on all the results described above, a plausible mechanism to understand the process of photoreforming hydrogen production over 2DC-TNS should consider the hole migration from the titania to the carbon material. In other words, we can assume that electrons can also be transferred from the carbon material to the titania. As discussed in the introduction, in photocatalysis field, with a few number of exceptions such as the work published by Saha et al. [24], carbon materials are generally considered as electron acceptors and used to facilitate electrons transport from one semiconductor to another or a co-catalyst such as Pt. In the case of the 2DC-TNS, we propose the following reaction mechanism, as illustrated in Fig. 17:

1) Once the TNS is illuminated by the light source, the electrons and holes are generated and then migrate to the surface of TNS.
2) As it was confirmed, the photogenerated electrons tend to migrate to the {101} facets, while the corresponding holes will accumulate on the {001} facets [48,49].
3) Platinum nanoparticles are photo-deposited mainly on the electron-rich {101} facets. These Pt nanoparticles act as the active sites for the reduction half-reaction where the hydrogen is produced.
4) Thanks to the good interface between the 2DC and the {101} facets of TNS, electrons of the carbon material move to the valence band of the TNS and effectively induces the hole migration from the TNS to the carbon.
5) Therefore, the photooxidation of ethanol occurs on either the expanded carbon or the {001} facets of TNS that are not in contact with the carbon. It is obvious that the first one regenerates the
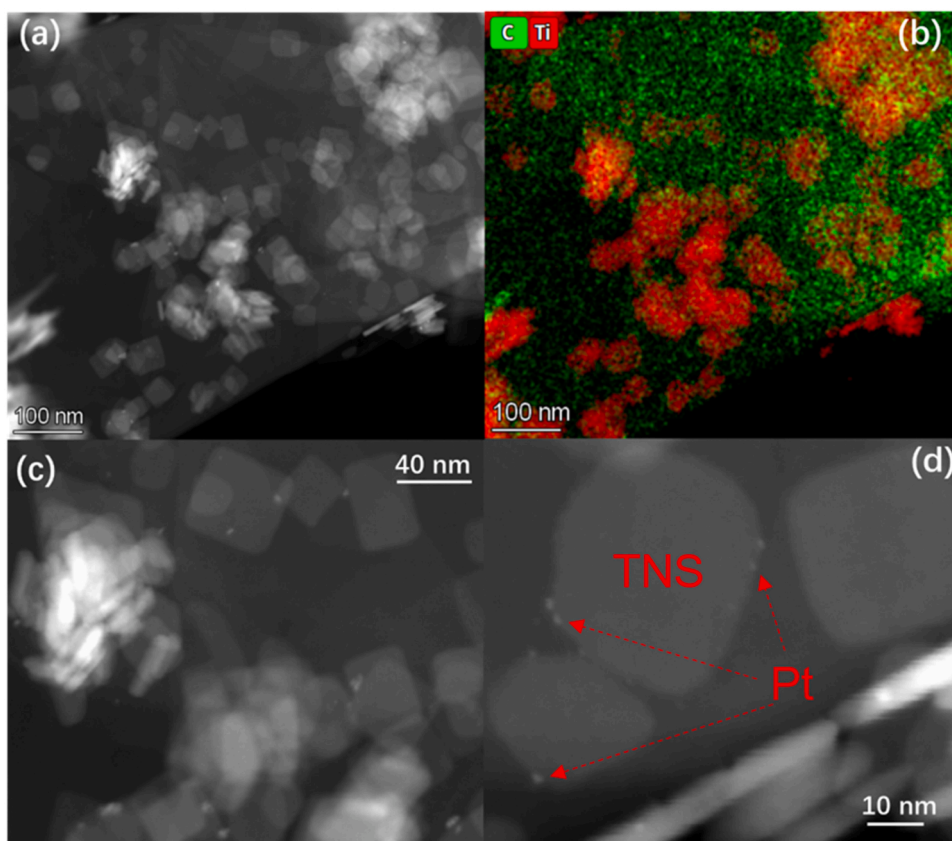
**Fig. 15.** Representative HAADF-STEM images of sample 2DC-TNS (a, c and d) and element mapping of image a (b) after photocatalytic test.
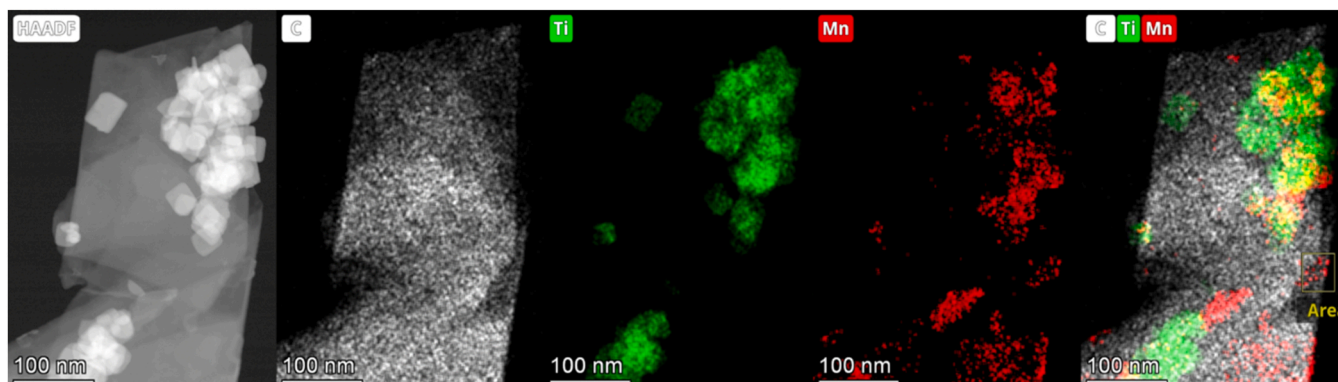


**Fig. 16.** HAADF-STEM image and corresponding element mapping of 2DC-TNS after MnO$_x$ photodeposition.

electrons previously transferred from the carbon to the TNS, thus closing the redox cycle.

It should be pointed out that, even though in the field of photocatalysis carbonaceous materials are only recognized as electron acceptor and carrier, we can find many examples of the use of carbonaceous materials as anode, where organic pollutants are directly oxidized into harmless substances. In a recent review, Jiang et al. highlights that the good conductivity, high specific surface area, and excellent adsorption capability are characteristic that makes the carbon an excellent candidate for anode in the anodic oxidation of organic pollutants [54]. In this sense, carbon materials will participate in the oxidation reaction, and may also facilitate the adsorption and activation of organic molecules. For example, Labiadh et al. found that a Boron-Doped Diamond (BDD) anode exhibited better activity that other

noble metal based electrodes for the anodic removal of pollutants [55]. Therefore, the use of carbon materials as hole carriers is a viable option, and the unique properties of carbon materials would facilitate the adsorption of the organic molecules that are used as sacrificial reagents in the photoreforming reaction.

A tentative band diagram is included in Fig. S18 based on the well-established band structure of anatase and the reduction potential of Mn$^{3+}$/Mn$^{2+}$ and Pt$^{2+}$/Pt. Comparing these values with the information about the reaction allows us to qualitatively determine the relative positions of the HOMO of the carbon material and the TiO$_2$. We should note that all the raw carbon materials are capable of photo-reducing Pt$^{2+}$ as observed in Table S2, indicating that some electrons located in the carbon should be higher than the redox potential of this reduction reaction. However, the Mn$^{2+}$ was mainly not oxidized to Mn$^{3+}$, indicating that the electrons in the HOMO level should be higher than this reaction.
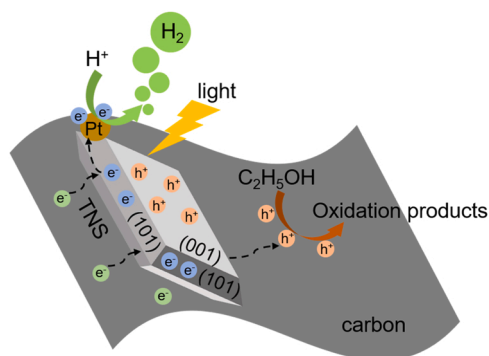
**Fig. 17.** The proposed mechanism for the photocatalytic improvement over 2DC-TNS system.

On the other hand, manganese was fully oxidized in the presence of $TiO_2$, indicating that the HOMO level is below the reduction potential of that reaction. Therefore, it is clear that electrons from either the HOMO level of the 2DC can move to the valence band of the titania, and the photo-excited electrons of the titania can be transferred to the carbon materials.

## 4. Conclusions

In summary, two types of carbon-titania hybrid photocatalyst systems were successfully prepared for photoreforming hydrogen production. In both cases, the presence of carbon materials enhanced the photocatalytic performance and according to the PL results, the improvement can be related with the spatial charge separation. Regarding to MWCNT-$TiO_2$ system, we found evidence that the spatial separation of charge carriers was achieved by the injection of photo-excited electrons from the titania to the MWCNTs, as supported by the observation of photodeposited Pt on the MWCNTs' surface and the $Mn_2O_3$ on the $TiO_2$. In contrast, the good interaction between the two-dimensional carbon and the {001} facets of TNS in 2DC-TNS system allowed for the migration of photogenerated holes from the TNS to the expanded carbon. Our results indicate that both charge carrier separation mechanisms are viable. If we consider the relative improvement on the photocatalytic performance, the promotion of the hole migration to the carbon material is a promising approach to improve the photocatalytic activity of titania.

## CRediT authorship contribution statement

JJ Delgado designed the experiments, obtained funding, performed TEM characterization and interpretation, and contributed to the discussion. JJ Delgado also wrote the initial draft with E. Bu and contributed to the discussion, J Martínez-López performed X-ray diffraction characterization and contributed to the discussion, C. López-Cartes performed XPS characterization and contributed to the discussion, E. Bu prepared the samples, performed catalytic tests, fluorescence characterization, and UV-Vis absorption, designed the experiments, wrote the draft witt JJ Delgado, and contributed to the discussion, X Chen obtained funding, designed the experiments and the idea, wrote the draft, and contributed to the discussion, F. Cazaña synthesized two-dimensional exfoliated carbon, A. Monzón obtained funding and contributed to the discussion, All authors have read and approved the final manuscript.

## Declaration of Competing Interest

The authors declare the following financial interests/personal relationships which may be considered as potential competing interests: Juan Jose Delgado reports financial support was provided by Spain

## Data availability

Data will be made available on request.

## Appendix A. Supporting information

Supplementary data associated with this article can be found in the online version at doi:10.1016/j.cattod.2023.114220.

## References

[1] M. Ji, J. Wang, Review and comparison of various hydrogen production methods based on costs and life cycle impact assessment indicators, Int. J. Hydrog. Energy 46 (2021) 38612–38635, https://doi.org/10.1016/j.ijhydene.2021.09.142.

[2] P.J. Megía, A.J. Vizcaíno, J.A. Calles, A. Carrero, Hydrogen production technologies: from fossil fuels toward renewable sources. a mini review, Energy Fuels 35 (2021) 16403–16415, https://doi.org/10.1021/acs.energyfuels.1c02501.

[3] M. Ji, J. Wang, Review and comparison of various hydrogen production methods based on costs and life cycle impact assessment indicators, Int. J. Hydrog. Energy 46 (2021) 38612–38635, https://doi.org/10.1016/j.ijhydene.2021.09.142.

[4] A. Fujishima, K. Honda, Electrochemical photolysis of water at a semiconductor electrode, Nature 238 (1972) 37–38, https://doi.org/10.1038/238037a0.

[5] X. Wang, X. Lü, More than biofuels: use ethanol as chemical feedstock, in: B.P. Lü (Ed.), Advances in 2nd Generation of Bioethanol Production, Woodhead Publishing, 2021, pp. 31–51, https://doi.org/10.1016/b978-0-12-818862-0.00001-7.

[6] T. Hisatomi, J. Kubota, K. Domen, Recent advances in semiconductors for photocatalytic and photoelectrochemical water splitting, Chem. Soc. Rev. 43 (2014) 7520–7535, https://doi.org/10.1039/c3cs60378d.

[7] A.V. Puga, Photocatalytic production of hydrogen from biomass-derived feedstocks, Coord. Chem. Rev. 315 (2016) 1–66, https://doi.org/10.1016/j.ccr.2015.12.009.

[8] M. Pelaez, N.T. Nolan, S.C. Pillai, M.K. Seery, P. Falaras, A.G. Kontos, P.S. M. Dunlop, J.W.J. Hamilton, J.A. Byrne, K. O'Shea, M.H. Entezari, D.D. Dionysiou, A review on the visible light active titanium dioxide photocatalysts for environmental applications, Appl. Catal. B Environ. 125 (2012) 331–349, https://doi.org/10.1016/j.apcatb.2012.05.036.

[9] N. Ramesh Reddy, U. Bhargav, M. Mamatha Kumari, K.K. Cheralathan, M. Sakar, Review on the interface engineering in the carbonaceous titania for the improved photocatalytic hydrogen production, Int. J. Hydrog. Energy 45 (2020) 7584–7615, https://doi.org/10.1016/j.ijhydene.2019.09.041.

[10] X.Z. Yue, C.Q. Li, Z.Y. Liu, S.S. Yi, D.L. Chen, F. Wang, S.H. Li, Steering charge kinetics in $W_2C@C/TiO_2$ heterojunction architecture: efficient solar-light-driven hydrogen generation, Appl. Catal. B Environ. 255 (2019), 117760, https://doi.org/10.1016/j.apcatb.2019.117760.

[11] M. Bernareggi, G.L. Chiarello, G. West, M. Ratova, A.M. Ferretti, P. Kelly, E. Selli, Cu and Pt clusters deposition on $TiO_2$ powders by DC magnetron sputtering for photocatalytic hydrogen production, Catal. Today 326 (2019) 15–21, https://doi.org/10.1016/j.cattod.2018.07.011.

[12] S.B. Patil, P.S. Basavarajappa, N. Ganganagappa, M.S. Jyothi, A.V. Raghu, K. R. Reddy, Recent advances in non-metals-doped $TiO_2$ nanostructured photocatalysts for visible-light driven hydrogen production, $CO_2$ reduction and air purification, Int. J. Hydrog. Energy 44 (2019) 13022–13039, https://doi.org/10.1016/j.ijhydene.2019.03.164.

[13] J.L. Faria WWang Carbon Materials in Photocatalysis P. Serp J.L. FigueiredoCarbon Materials for Catalysis 2008 John Wiley & Sons, Inc New York 481 506 https://doi.org/10.1002/9780470403709.ch13.

[14] J. Schneider, M. Matsuoka, M. Takeuchi, J. Zhang, Y. Horiuchi, M. Anpo, D. W. Bahnemann, Understanding $TiO_2$ photocatalysis: mechanisms and materials, Chem. Rev. 114 (2014) 9919–9986, https://doi.org/10.1021/cr5001892.

[15] N. Naffati, M.J. Sampaio, E.S. Da Silva, M.F. Nsib, Y. Arfaoui, A. Houas, J.L. Faria, C.G. Silva, Carbon-nanotube/$TiO_2$ materials synthesized by a one-pot oxidation/hydrothermal route for the photocatalytic production of hydrogen from biomass derivatives, Mater. Sci. Semicond. Process. 115 (2020), 105098, https://doi.org/10.1016/j.mssp.2020.105098.

[16] S. Singla, S. Sharma, S. Basu, N.P. Shetti, T.M. Aminabhavi, Photocatalytic water splitting hydrogen production via environmental benign carbon based

nanomaterials, Int. J. Hydrog. Energy 46 (2021) 33696–33717, https://doi.org/10.1016/j.ijhydene.2021.07.187.

[17] M.R. Karimi Estahbanati, M. Feilizadeh, M. Shokrollahi Yancheshmeh, M.C. Iliuta, Effects of carbon nanotube and carbon sphere templates in $TiO_2$ composites for photocatalytic hydrogen production, Ind. Eng. Chem. Res. 58 (2019) 2770–2783, https://doi.org/10.1021/acs.iecr.8b05815.

[18] J. Yu, B. Yang, B. Cheng, Noble-metal-free carbon nanotube-$Cd_{0.1}Zn_{0.9}S$ composites for high visible-light photocatalytic $H_2$-production performance, Nanoscale 4 (2012) 2670–2677, https://doi.org/10.1039/c2nr30129f.

[19] K. Woan, G. Pyrgiotakis, W. Sigmund, Photocatalytic carbon-nanotube-$TiO_2$ composites, Adv. Mater. 21 (2009) 2233–2239, https://doi.org/10.1002/adma.200802738.

[20] C. Dong, X. Li, P. Jin, W. Zhao, J. Chu, J. Qi, Intersubunit electron transfer (IET) in quantum dots/graphene complex: What features does IET endow the complex with? J. Phys. Chem. C. 116 (2012) 15833–15838, https://doi.org/10.1021/jp304624y.

[21] Z. Lian, P. Xu, W. Wang, D. Zhang, S. Xiao, X. Li, G. Li, $C_{60}$-decorated CdS/$TiO_2$ mesoporous architectures with enhanced photostability and photocatalytic activity for $H_2$ evolution, ACS Appl. Mater. Interfaces 7 (2015) 4533–4540, https://doi.org/10.1021/am5088665.

[22] A. Iwase, Y.H. Ng, Y. Ishiguro, A. Kudo, R. Amal, Reduced graphene oxide as a solid-state electron mediator in Z-scheme photocatalytic water splitting under visible light, J. Am. Chem. Soc. 133 (2011) 11054–11057, https://doi.org/10.1021/ja203296z.

[23] K.H. Jung, J.S. Hong, R. Vittal, K.J. Kim, Enhanced photocurrent of dye-sensitized solar cells by modification of $TiO_2$ with carbon nanotubes, Chem. Lett. 31 (2002) 864–865, https://doi.org/10.1246/cl.2002.864.

[24] A. Saha, A. Moya, A. Kahnt, D. Iglesias, S. Marchesan, R. Wannemacher, M. Prato, J.J. Vilatela, D.M. Guldi, Interfacial charge transfer in functionalized multi-walled carbon nanotube@$TiO_2$ nanofibres, Nanoscale 9 (2017) 7911–7921, https://doi.org/10.1039/c7nr00759k.

[25] S. Lettieri, V. Gargiulo, D.K. Pallotti, G. Vitiello, P. Maddalena, M. Alfè, R. Marotta, Evidencing opposite charge-transfer processes at $TiO_2$/graphene-related materials interface through combined EPR, photoluminescence and photocatalysis assessment, Catal. Today 315 (2018) 19–30, https://doi.org/10.1016/j.cattod.2018.01.022.

[26] F. Wang, K. Matsuda, Applications of carbon nanotubes in solar cells, in: N. Nakashima (Ed.), Nanostructure Sci. Technol., Springer International Publishing, Cham, 2019, pp. 497–536, https://doi.org/10.1007/978-3-319-92917-0_20.

[27] M. Catauro, E. Tranquillo, G. Dal Poggetto, M. Pasquali, A. Dell'Era, S.V. Ciprioti, Influence of the heat treatment on the particles size and on the crystalline phase of $TiO_2$ synthesized by the sol-gel method, Materials 11 (2018) 2364, https://doi.org/10.3390/ma11122364.

[28] J. Yu, L. Qi, M. Jaroniec, Hydrogen production by photocatalytic water splitting over Pt/$TiO_2$ nanosheets with exposed (001) facets, J. Phys. Chem. C. 114 (2010) 13118–13125, https://doi.org/10.1021/jp104488b.

[29] H. Pan, X. Chen, O. Sanz, M.A. Cauqui, J.M. Rodríguez-Izquierdo, J.J. Delgado, A facile one-pot hydrothermal synthesis as an efficient method to modulate the potassium content of cryptomelane and its effects on the redox and catalytic properties, Chin. J. Catal. 40 (2019) 940–952, https://doi.org/10.1016/S1872-2067(19)63339-5.

[30] M. Luna, J.J. Delgado, I. Romero, T. Montini, M.L. Almoraima Gil, J. Martínez-López, P. Fornasiero, M.J. Mosquera, Photocatalytic $TiO_2$ nanosheets-$SiO_2$ coatings on concrete and limestone: an enhancement of de-polluting and self-cleaning properties by nanoparticle design, Constr. Build. Mater. 338 (2022), 127349, https://doi.org/10.1016/j.conbuildmat.2022.127349.

[31] J.C. Groen, L.A.A. Peffer, J. Pérez-Ramírez, Pore size determination in modified micro- and mesoporous materials. Pitfalls and limitations in gas adsorption data analysis, Microporous Mesoporous Mater. 60 (2003) 1–17, https://doi.org/10.1016/S1387-1811(03)00339-1.

[32] Z. Shan, Y. He, N. Liu, J. Li, M. Li, Y. Zhang, Spontaneously rooting carbon nanotube incorporated N-doped carbon nanofibers as efficient sulfur host toward high performance lithium-sulfur batteries, Appl. Surf. Sci. 539 (2021), 148209, https://doi.org/10.1016/j.apsusc.2020.148209.

[33] R. Wang, H. Wu, R. Chen, Y. Chi, Strong Electrochemiluminescence Emission from Oxidized Multiwalled Carbon Nanotubes, Small 15 (2019), 1901550, https://doi.org/10.1002/smll.201901550.

[34] J.P. Tessonnier, D. Rosenthal, T.W. Hansen, C. Hess, M.E. Schuster, R. Blume, F. Girgsdies, N. Pfänder, O. Timpe, D.S. Su, R. Schlögl, Analysis of the structure and chemical properties of some commercial carbon nanostructures, Carbon 47 (2009) 1779–1798, https://doi.org/10.1016/j.carbon.2009.02.032.

[35] S. Bellamkonda, N. Thangavel, H.Y. Hafeez, B. Neppolian, G. Ranga Rao, Highly active and stable multi-walled carbon nanotubes-graphene-$TiO_2$ nanohybrid: An

efficient non-noble metal photocatalyst for water splitting, Catal. Today 321–322 (2019) 120–127, https://doi.org/10.1016/j.cattod.2017.10.023.

[36] G.D. Gesesse, A. Gomis-Berenguer, M.F. Barthe, C.O. Ania, On the analysis of diffuse reflectance measurements to estimate the optical properties of amorphous porous carbons and semiconductor/carbon catalysts, J. Photochem. Photobiol. A Chem. 398 (2020), 112622, https://doi.org/10.1016/j.jphotochem.2020.112622.

[37] L.L. Qu, N. Wang, Y.Y. Li, D.D. Bao, G.H. Yang, H.T. Li, Novel titanium dioxide–graphene–activated carbon ternary nanocomposites with enhanced photocatalytic performance in rhodamine B and tetracycline hydrochloride degradation, J. Mater. Sci. 52 (2017) 8311–8320, https://doi.org/10.1007/s10853-017-1047-0.

[38] C.C. Mercado, F.J. Knorr, J.L. McHale, S.M. Usmani, A.S. Ichimura, L.V. Saraf, Location of hole and electron traps on nanocrystalline anatase $TiO_2$, J. Phys. Chem. C. 116 (2012) 10796–10804, https://doi.org/10.1021/jp301680d.

[39] R.E. Rex, F.J. Knorr, J.L. McHale, Comment on characterization of oxygen vacancy associates within hydrogenated $TiO_2$: a positron annihilation study, J. Phys. Chem. C. 117 (2013) 7949–7951, https://doi.org/10.1021/jp402351u.

[40] J.L. McHale, F.J. Knorr, Photoluminescence and Carrier Transport in Nanocrystalline $TiO_2$, in: L Bergman, J.L. McHale (Eds.), Handbook of Luminescent Semiconductor Materials, CRC Press, Boca Raton, 2016, pp. 365–390, https://doi.org/10.1201/b11201.

[41] M.A. Esteves, F. Fresno, V.R. Fernandes, F.E. Oropeza, V.A. de la Peña O'Shea, C. M. Rangel, $TiO_2$-reduced graphene oxide-Pt nanocomposites for the photogeneration of hydrogen from ethanol liquid and gas phases, Catal. Today 380 (2021) 41–52, https://doi.org/10.1016/j.cattod.2021.05.012.

[42] R. Li, F. Zhang, D. Wang, J. Yang, M. Li, J. Zhu, X. Zhou, H. Han, C. Li, Spatial separation of photogenerated electrons and holes among {010} and {110} crystal facets of $BiVO_4$, Nat. Commun. 4 (2013) 1423, https://doi.org/10.1038/ncomms2401.

[43] A. Gloter, C. Ewels, P. Umek, D. Arcon, C. Colliex, Electronic structure of titania-based nanotubes investigated by EELS spectroscopy, Phys. Rev. B - Condens. Matter Mater. Phys. 80 (2009) 1–6, https://doi.org/10.1103/PhysRevB.80.035413.

[44] Y. Guo, Q. Zhou, J. Nan, W. Shi, F. Cui, Y. Zhu, Perylenetetracarboxylic acid nanosheets with internal electric fields and anisotropic charge migration for photocatalytic hydrogen evolution, Nat. Commun. 13 (2022) 2067, https://doi.org/10.1038/s41467-022-29826-z.

[45] R.M. Navarro, J. Arenales, F. Vaquero, I.D. González, J.L.G. Fierro, The effect of Pt characteristics on the photoactivity of Pt/$TiO_2$ for hydrogen production from ethanol, Catal. Today 210 (2013) 33–38, https://doi.org/10.1016/j.cattod.2013.01.006.

[46] A.V. Puga, A. Forneli, H. García, A. Corma, Production of $H_2$ by ethanol photoreforming on Au/$TiO_2$, Adv. Funct. Mater. 24 (2014) 241–248, https://doi.org/10.1002/adfm.201301907.

[47] R. Leary, A. Westwood, Carbonaceous nanomaterials for the enhancement of $TiO_2$ photocatalysis, Carbon 49 (2011) 741–772, https://doi.org/10.1016/j.carbon.2010.10.010.

[48] J. Pan, G. Liu, G.Q. Lu, H.M. Cheng, On the true photoreactivity order of {001}, {010}, and {101} facets of anatase $TiO_2$ crystals, Angew. Chem. - Int. Ed. 50 (2011) 2133–2137, https://doi.org/10.1002/anie.201006057.

[49] X. Liu, G. Dong, S. Li, G. Lu, Y. Bi, Direct observation of charge separation on anatase $TiO_2$ crystals with selectively etched {001} facets, J. Am. Chem. Soc. 138 (2016) 2917–2920, https://doi.org/10.1021/jacs.5b12521.

[50] L. Yang, R. Wang, N. Zhou, L. Jiang, H. Liu, Q. He, C. Deng, D. Chu, M. Zhang, Z. Sun, Construction of p-n heterostructured BiOI/$TiO_2$ nanosheets arrays for improved photoelectrochemical water splitting performance, Appl. Surf. Sci. 601 (2022), 154277, https://doi.org/10.1016/j.apsusc.2022.154277.

[51] D.M. Guldi, G.M.A. Rahman, N. Jux, D. Balbinot, N. Tagmatarchis, M. Prato, Multiwalled carbon nanotubes in donor-acceptor nanohybrids - Towards long-lived electron transfer products, Chem. Commun. (2005) 2038–2040, https://doi.org/10.1039/b418406h.

[52] J. Ji, Y. Zhang, L. Tang, C. Liu, X. Gao, M. Sun, J. Zheng, M. Ling, C. Liang, Z. Lin, Platinum single-atom and cluster anchored on functionalized MWCNTs with ultrahigh mass efficiency for electrocatalytic hydrogen evolution, Nano Energy 63 (2019), 103849, https://doi.org/10.1016/j.nanoen.2019.06.045.

[53] J. Ma, A. Habrioux, A. Pisarek, A. Lewera, N. Alonso-Vante, Induced electronic modification of Pt nanoparticles deposited onto graphitic domains of carbon materials by UV irradiation, Electrochem. Commun. 29 (2013) 12–16, https://doi.org/10.1016/j.elecom.2012.12.028.

[54] Y. Jiang, H. Zhao, J. Liang, L. Yue, T. Li, Y. Luo, Q. Liu, S. Lu, A.M. Asiri, Z. Gong, X. Sun, Anodic oxidation for the degradation of organic pollutants: anode materials, operating conditions and mechanisms. A mini review, Electrochem. Commun. 123 (2021), 106912, https://doi.org/10.1016/j.elecom.2020.106912.

[55] L. Labiadh, A. Barbucci, G. Cerisola, A. Gadri, S. Ammar, M. Panizza, Role of anode material on the electrochemical oxidation of methyl orange, J. Solid State Electrochem 19 (2015) 3177–3183, https://doi.org/10.1007/s10008-015-2928-2.